Self-assembled charged hydrogels control the alignment of filamentous actin†

Jung Hyun Park,[ab] Yujie Sun,[bc] Yale E. Goldman[bc] and Russell J. Composto*[ab]

Received 4th September 2009, Accepted 30th November 2009
First published as an Advance Article on the web 21st December 2009
DOI: 10.1039/b918304c

We demonstrate a novel route to control attachment of filamentous actin (F-actin) on hydrogel films. By incorporating an amine-terminated silane, the hydrogel surface charge and surface topography are varied. With increasing silane content, F-actin reorients from perpendicular to parallel to the hydrogel surface, ceases to wobble, and forms mainly elongated or cyclic structures. F-Actin coverage reaches a maximum at 2.5 vol% silane and declines at higher silane content. This biphasic behavior is explained by the simultaneous increase in surface charge and the self-assembly of a micron scale pattern of positively charged islands. Our approach provides guidelines for constructing nanoscale tracks to guide motor proteins underlying nano-engineered devices such as molecular shuttles.

Introduction

Motor proteins have the ability to transport cargo on surfaces,[1] stretch and transport DNA molecules,[2] and perform other manipulations of nanoscale components.[3] These motor proteins move along tracks of biofilaments, actin and microtubules, which are two major components of the cytoskeleton of biological cells. Thus, in conjunction, biofilaments and molecular motors underlie how cells generate forces necessary for tasks from cell motility and division to intracellular transport.[4–6] Nano-biotechnology is looking at whether these molecular machines can be mimicked or recruited to create new devices. In this paper, we focus on understanding how the tracks (*i.e.*, biofilaments) that guide the motion of motor proteins are attached to "soft" surfaces.

F-Actin can be found in various geometries: single filaments, bundles, and complex networks that are regulated by actin binding proteins (ABPs) and ionic conditions.[7–11] The polymorphism of F-actin can be understood by considering the binding partner and electrostatic interactions underlying this polyelectrolyte in solution. For example, Janmey and Tang[7,8] studied the effect of polycations on bundle formation of F-actin and found that a critical concentration of ions is required to induce bundling. By modeling actin as a charged rod in the presence of linker proteins, Liu *et al.*[9] predicted the structural arrangements that lead to the formation of isotropic, nematic, cubatic, and bundle phases. These predictions were later confirmed by synchrotron X-ray scattering experiments.[10,11] While these studies help us to understand how F-actin assembles in buffered aqueous media, the organization of F-actin on surfaces has received relatively little attention.

The interaction between F-actin and a surface is particularly important for understanding molecular motors, such as myosin. For example, controlled immobilization of F-actin enables various fluorescence techniques to be used to study real-time motion and orientation of myosin.[12–14] In these studies, specific interactions such as streptavidin–biotin binding are used to immobilize F-actin. Furthermore, researchers have recently focused on selective attachment and alignment of F-actin on surfaces.[15,16] For example, F-actin has been elongated on *N*-ethylmaleimide-modified myosin tracks patterned by microcontact printing.[15] At the nanoscale, the selective attachment of F-actin was performed on amphiphilic block copolymer templates.[16] In this block copolymer study, electrostatic interactions were successfully used to control attachment by taking advantage of F-actin's attributes as a negatively charged polyelectrolyte. In addition, electric fields, shear flow, and physical confinement have also been used to align F-actin.[17–21] One might utilize such patterned molecular motor-cytoskeleton systems in molecular shuttle devices for the transportation of cargos which can be tethered to the molecular motor.[22–27]

As biocompatible materials, hydrogels exhibit flexible and variable properties that are advantageous for regulating cell function and adhesion.[28–32] Topographically patterned hydrogel substrates have been used to control cell alignment, which involves cytoskeletal organization along the pattern direction.[33,34] To study extracellular patterning of actin, we developed hydrogel films with tunable surface charge and topographical characteristics. Depending on the magnitude of charge and the periodicity of the surface pattern, we can control the adhesion of F-actin as well as vary F-actin orientation, interaction strength, surface coverage, and curvature.

We prepared self-assembled charged hydrogel films by stabilizing poly(acrylic acid) (PAA) films with 3-aminopropyltriethoxysilane (APTES). A PAA film physisorbed on glass or silicon oxide partially desorbs in water and exhibits a net negative charge. However, upon cross-linking by APTES, PAA becomes a gel firmly attached to the substrate and positively charged due to the incorporation of amine groups.[16] This cross-linking and charge inversion of PAA was utilized in a prior study in which PAA was confined to nanoscale domains that served as

[a]*Department of Materials Science and Engineering, University of Pennsylvania, Philadelphia, Pennsylvania, 19104-6272, USA. E-mail: composto@seas.upenn.edu; Fax: +1 215 573 2128; Tel: +1 215 898 4451*
[b]*Nano/Bio Interface Center, University of Pennsylvania, Philadelphia, Pennsylvania, 19104-6272, USA*
[c]*Pennsylvania Muscle Institute, University of Pennsylvania, Philadelphia, Pennsylvania, 19104-6083, USA*

† Electronic supplementary information (ESI) available: Real-time TIRFM movies of fluorescently labeled F-actin on hydrogel films. See DOI: 10.1039/b918304c

anchoring sites for attaching F-actin.[16] The carboxylic acid groups in PAA were shown to react with some amine groups in APTES. Moreover, free siloxane groups cross-linked with each other and free amines produced positive charges on the surface that attracted actin. Whereas these experiments demonstrate that F-actin can be attracted to APTES stabilized PAA nanodomains (APTES–PAA), a systematic variation of substrate properties (*i.e.*, charge and topography) was not undertaken and therefore the underlying mechanism of F-actin attachment was not resolved.

Here, we show that a self-assembled hydrogel film of APTES–PAA provides a method to systematically vary the surface charge and surface topography that determine the orientation and adhesion of F-actin. As APTES concentration increases, F-actin reorients from perpendicular to parallel to the hydrogel surface, ceases to wobble, and becomes highly aligned. Concurrently, F-actin coverage initially increases, reaches a maximum at intermediate APTES concentration, and then decreases. This biphasic behavior is explained by an increase in electrostatic attraction due to the surface charge that occurs in parallel with an increase in surface heterogeneity as APTES concentration increases.

Experimental

Preparation of hydrogel films

PAA films were obtained by thermal deprotection of poly(*tert*-butyl acrylate) (P*t*BA) films. P*t*BA (M_w = 39.5 kDa) was purchased from Polymer Source Inc. Before film deposition, silicon wafers and glass microscope slides were treated with a piranha solution (98% H_2SO_4 : 30% H_2O_2 = 3 : 1 v/v) at 80 °C for 30 min followed by rinsing in deionized water (Millipore Direct-Q, 18 MΩ cm resistivity). After immersion in water for 1 day, substrates were dried by nitrogen gas. To remove organic residues and produce surface hydroxyl groups, the surfaces were exposed to UV-ozone (Model 42 Cleaner, Jelight Company Inc.) for 10 min. Films were prepared by spin casting polymer solutions (1 wt% in toluene) and annealing at 160 °C in vacuum for 2 days. The film thicknesses were measured by ellipsometry (Rudolf Research AutoEL-II Null ellipsometer). The film thickness decreased from 40 nm to 17 nm during the chemical transformation of P*t*BA to PAA. APTES–PAA films were prepared by immersing PAA films in buffer solutions containing APTES at various concentrations (0.1%, 1%, 2.5%, 5%, and 20%) for 1 h, and then washing with deionized water. We denote the cross-linked PAA films in terms of the volume percent of APTES in the buffer solution, (*i.e.*, *x*% APTES–PAA). In a prior study,[16] we have measured film thickness of neat PAA and APTES (0.5 vol%) stabilized PAA and observed an increase from 19 nm to 50 nm. Whereas the unmodified PAA almost completely desorbs into buffer, the PAA stabilized by APTES swells by 2.6 times.

Preparation of F-actin

Globular (G-) actin was isolated and purified from rabbit muscle as described by Pardee and Spudich[35] and stored in G-actin buffer (2 mM Tris buffer (pH 8.0), 0.2 mM $CaCl_2$, 0.2 mM ATP and 0.5 mM DTT). To prepare 1 μM rhodamine phalloidin stabilized F-actin, 1 μM G-actin was mixed gently with 4× F-actin buffer (300 mM KCl, 10 mM $MgCl_2$, 40 mM HEPES (pH 7.0), accounting for ¼ of the total volume) and 1.1 μM rhodamine phalloidin (Molecular Probes, R415), incubated at room temperature for 10 min, transferred onto ice, stored at 4 °C, and used within 1 month.[36] M5 buffer solution (25 mM KCl, 20 mM HEPES (pH 7.6), 2 mM $MgCl_2$, 1 mM EGTA (Sigma, E4378)) was used for all aqueous experiments.

TIRFM and SPM

Total internal reflection fluorescence microscopy (TIRFM) was used to image fluorescently labeled F-actin. In order to obtain a convenient surface density, F-actin was diluted 5 fold (final concentration: 200 nM) in M5 buffer. A flow chamber was constructed by assembling a 24 mm × 40 mm coverslip (Fisher) and a glass slide using double-sided adhesive tape. Sample chambers contained approximately 20 μl of solution. Rhodamine labeled F-actin was flowed into this chamber, incubated for 5 min and then unbound actin was washed away. Subsequently, the TIRFM images were taken in M5 buffer. To observe the surface morphologies of hydrogel films, scanning probe microscopy (SPM) was used. Films were prepared by drying for 1 day in a loosely covered Petri dish and imaged under ambient conditions. The images were analyzed by taking 2D fast Fourier transforms (FFTs) using Picoimage software.

Zeta potential

In the zeta potential method, a closed liquid cell was used to determine the surface zeta potential of hydrogel films prepared at various APTES concentrations. When an electric field is applied across the cell, colloidal particles of known zeta potential flow across the channel. In addition, this electric field induces an electro-osmotic flow in the cell due to the counter ions adjacent to the charged surface of sample. Thus, the apparent mobility of colloids (measured) is equal to the sum of the true mobility (known) and electro-osmotic flow (unknown). By determining the flow term, the magnitude and sign of the average surface zeta potential of the hydrogel can be determined. Because flow occurs across the entire surface (37 mm × 16 mm), this method is only sensitive to the average surface charge and insensitive to local heterogeneities.

Results and discussion

To study the adhesion of negatively charged F-actin to the surfaces, we incubated solutions containing F-actin on PAA, 0.1% APTES–PAA, 1% APTES–PAA, 2.5% APTES–PAA, 5% APTES–PAA, and 20% APTES–PAA films. Real-time TIRFM showed that actin filaments were tethered by their ends to the uncross-linked PAA film and extended away from the surface (Fig. 1(a)). The F-actin wobbled rapidly above the surface as demonstrated by the sequence of images (circles). A continuous series of TIRFM images (total time = 4 s) are available in the ESI†. As described later, this weak attraction is consistent with a balance between the van der Waals attraction and electrostatic repulsion acting between F-actin and the PAA surface.

Upon exposing PAA to a low concentration of APTES (0.1%), F-actin attaches parallel to the 0.1% APTES–PAA film (Fig. 1(b)), presumably by electrostatic attraction between negatively charged actin and free amines. The actin appears

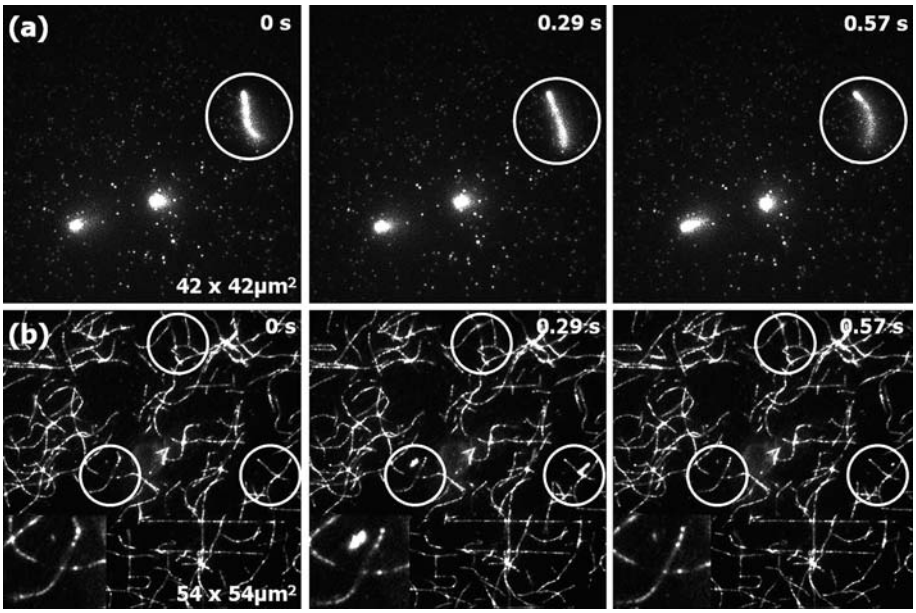

Fig. 1 Real-time TIRFM images show three time frames: 0, 0.29, and 0.57 s. (a) On a PAA film, fluorescently labeled F-actin is tethered at one end and thermally fluctuates in the buffer solution (actin highlighted in the circles). (b) On a 0.1% APTES–PAA film, actin is tethered parallel to the surface and fluctuates across the surface (filaments highlighted in the circles). Lower left circles are magnified for clarification in the insets.

weakly immobilized because sections, such as those indicated by the circles, continue to fluctuate over the surface. A series of TIRFM images (total time = 4 s) are provided in the ESI†. Thus by incorporating APTES into the PAA film, we change the orientation of F-actin, from perpendicular to parallel relative to the surface, and increase the contact area between the actin and the surface.

Upon stabilizing PAA with 1% APTES or more, actin becomes strongly attached to the hydrogel (Fig. 2). The real-time TIRFM movies (ESI†) show that F-actin is immobile. On 1% APTES–PAA and 2.5% APTES–PAA films (Fig. 2(a) and (b), respectively), a high surface coverage of actin is observed and many filaments are highly curved. Upon increasing the APTES concentration to 5% and 20% (Fig. 2(c) and (d), respectively), the actin coverage decreases and most filaments appear highly elongated in the direction of flow. This result was surprising because an increase in APTES concentration was expected to produce a corresponding increase in positive surface charge on the hydrogel. In addition, highly curved F-actin "rings" (diameter 2–6 μm) are observed in Fig. 2(c) and (d). This bending indicates considerable stress in the filament because the persistence length is ~15 μm.[37] Various F-actin rings are presented in the ESI†. Ring and loop configurations of actin were observed previously in buffer solution due to counterion condensation when a high concentration (50 mM) of divalent cations was added to dilute solutions of F-actin (5 nM).[38,39] The addition of dextran has also been shown to produce rings of actin filaments in solution, presumably due to excluded volume effects.[39] Actin rings are generated here by an alternative mechanism on surfaces using hydrogels.

To further understand how F-actin interacts with the hydrogel, the surface morphology, surface roughness and lateral periodicity of features on the hydrogel were characterized by SPM (Fig. 3). For the PAA, 0.1% APTES–PAA, 1% APTES–PAA, 2.5% APTES–PAA, 5% APTES–PAA, and 20% APTES–PAA films, the RMS roughness values are 0.25 nm, 1.0 nm, 1.4 nm, 2.7 nm, 2.7 nm, and 5.9 nm, respectively. Qualitatively, the lateral periodicity of the surface features jumps from the nanoscale at low APTES (≤2.5%) to the microscale at high APTES concentrations (≥5%). The microscale features, as shown in Fig. 3(f), are likely due to excess APTES molecules that aggregate in solution and deposit on the surface during the

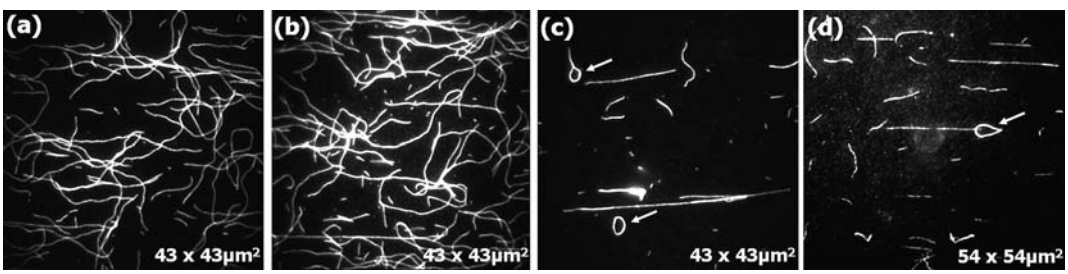

Fig. 2 F-Actin is immobilized on surfaces ranging from 1 to 20% APTES. (a) 1% APTES–PAA and (b) 2.5% APTES–PAA films show higher surface coverage and more curvature of F-actin than on the (c) 5% APTES–PAA and (d) 20% APTES–PAA films. Actin rings and loops are observed at the highest APTES concentrations (arrows in (c) and (d)).

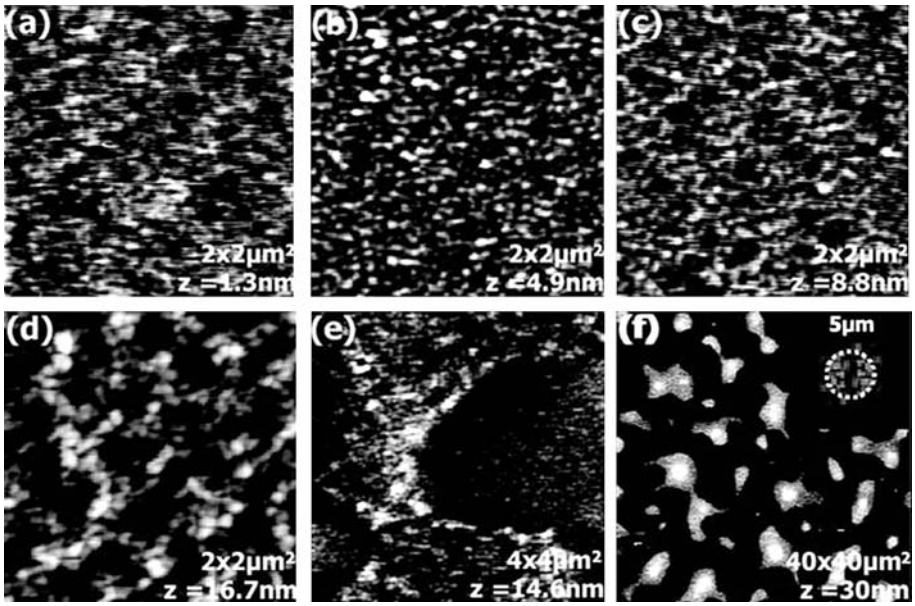

Fig. 3 SPM images of (a) PAA, (b) 0.1% APTES–PAA, (c) 1% APTES–PAA, (d) 2.5% APTES–PAA, (e) 5% APTES–PAA, and (f) 20% APTES–PAA surfaces. Patterns of APTES-rich features increase from the nanometre to micrometre scale as APTES concentration increases. FFTs are used to calculate the periodicity of the surface pattern (Fig. 4(a)) as shown in the inset of (f).

cross-linking reaction. The formation of APTES aggregates is well known and their size depends on the experimental conditions.[40] Also in Fig. 3(f), the aggregate height of the features is much less than their diameters; therefore, these aggregates form a random pattern of irregularly shaped pancake-like features on the surface of the hydrogel.

The microscale pattern of domains observed at 5 and 20% APTES may explain the decrease in surface coverage of F-actin shown in Fig. 4(a). Namely at high APTES concentrations, the dominant features are large positively charged islands (diameter 2–7 μm) which are comparable in size to the diameter of the actin rings and loops observed in the TIRFM images (Fig. 2(c) and (d)). The strong attraction of actin towards these islands, relative to areas between the islands, is presumably sufficient to overcome the energy penalty for bending the semi-flexible filament. Whereas some are highly curved, other filaments are strongly oriented along the flow direction. These filaments appear to straddle the positively charged islands by stretching along the direction of flow and become pinned. Thus, the micro-patterned arrangement of APTES islands observed at high APTES concentration is likely responsible for the decrease in F-actin coverage as well as the curved and elongated filaments.

A quantitative analysis of TIRFM and SPM images was performed to determine how the surface coverage and curvature of F-actin are related to the periodicity of the surface pattern and the surface charge of the hydrogel. Actin coverage (%) is defined as the number of pixels occupied by the fluorescence of actin filaments divided by the total number of pixels in the image area. Note that the real diameter of a single filament is 8 nm[37] whereas the average width measured in the TIRFM image is ~400 nm due to the limited resolution. Thus, the reported values represent the relative coverage of actin on the surfaces. As shown in Fig. 4(a), the coverage by F-actin increases until 2.5% APTES, significantly decreases up to 5% APTES, and then remains constant at a value of ~4% coverage. This behavior correlates with the periodicity of the surface patterns on APTES–PAA films. FFT analysis was used to calculate the lateral periodicity, L, of the features on the surface of the hydrogel (Fig. 4(a)). In particular, the sudden decrease of F-actin coverage between 2.5 and 5% coincides with an order of magnitude increase in lateral period, which jumps from the nano to microscale. The relative straightness of actin is quantified by plotting the end-to-end distance divided by the contour length ($L_{ee}/L_{contour}$) as a function of APTES concentration as shown in Fig. 4(b). Note that even for the 0.1% APTES–PAA substrate, F-actin is aligned by the flow field. As APTES concentration increases, $L_{ee}/L_{contour}$ increases rapidly and then approaches 1 (essentially straight filaments) at 20% APTES. In these measurements, F-actin rings were excluded. In summary, self-assembled patterns of APTES on the surface of hydrogels influence both the coverage and curvature of F-actin.

To quantify the hydrogel surface charge, zeta potential (ζ) measurements were performed. Fig. 5 shows that PAA alone exhibits a negative zeta potential of −16 mV. The lightly modified 0.1% APTES–PAA film also shows a negative zeta potential although its value is only −1.5 mV. Above 1% APTES, the zeta potentials become positive and approach +21 mV at 20% APTES. Thus, by exposing PAA to increasing amounts of APTES, more free amines are incorporated into the film. Correspondingly, this increase in positive surface charge results in a stronger electrostatic interaction between the negatively charged actin and the hydrogel, which is in qualitative agreement with the adsorption behavior observed in TIRFM experiments. Note that the zeta potential reflects an average surface charge density and does not capture the heterogeneity of charge distribution.

Using these zeta potential values, the interaction energy between F-actin and APTES–PAA films can be estimated. To make the problem tractable, the surface charge is assumed to be uniformly distributed across a smooth planar surface. This model considers the long-range electrostatic and short-range

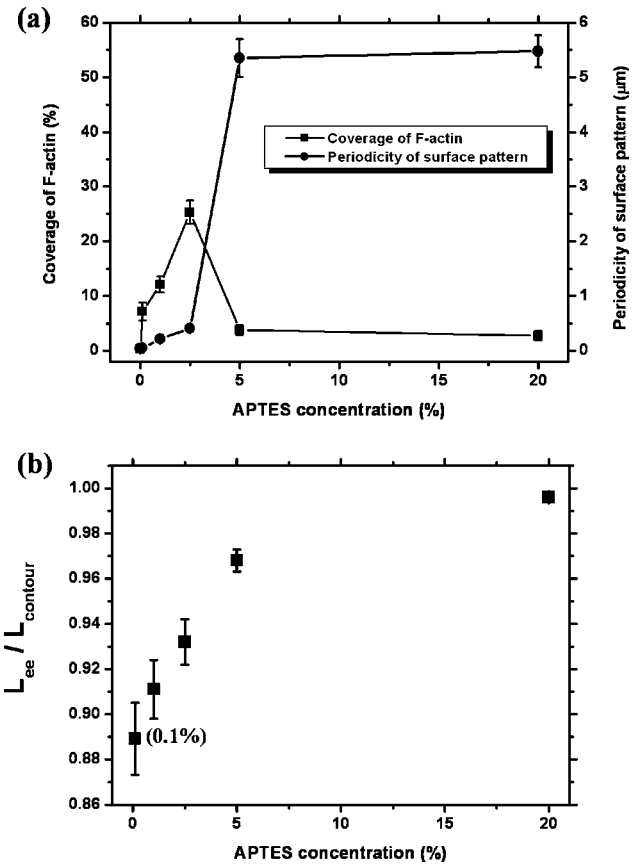

Fig. 4 (a) Coverage of F-actin increases up to 2.5% APTES and significantly drops at 5% APTES. Above 5% APTES, the coverage is constant over the experimental range. Note that the sudden decrease of F-actin coverage between 2.5% and 5% APTES coincides with a significant increase in lateral periodicity, from the nano to the micrometre scale. (b) Straightness of F-actin is quantified by plotting the end-to-end distance divided by the contour length ($L_{ee}/L_{contour}$) of each actin filament. As APTES concentration increases, the filaments become straighter. At 20% APTES, F-actin is very straight as noted by $L_{ee}/L_{contour} \approx 1$. In these measurements, F-actin rings were excluded.

van der Waals interactions between a cylindrical filament and the planar substrate.[41,42] The total interaction energy per unit length of F-actin is calculated as a function of distance, H, between the substrate and bottom of the cylinder for APTES concentrations up to 20%. Given the ionic concentrations, [KCl] = 25 mM, [$MgCl_2$] = 2 mM, and charge neutrality condition, 2[Mg^{2+}] = [Cl^-], the Debye length, κ^{-1}, is calculated[42] from $\kappa^{-1} = (\Sigma_i z_i^2 \rho_i e^2/\varepsilon_{water}\varepsilon_0 kT)^{-1/2} = 1.7$ nm, where z_i is the valency of ions i, ρ_i is the ionic concentration of ions i in the bulk, e is the elementary charge, ε_{water} is the relative permittivity of water, ε_0 is the vacuum permittivity, k is Boltzmann constant, and T is the absolute temperature. The relative permittivities of APTES–PAA films and F-actin are both assumed to be $\varepsilon_{APTES-PAA} = \varepsilon_{actin} = 15$. From the known surface charge of F-actin, $\sigma = -0.02$ C m^{-2}, the surface potential of F-actin (Ψ_{actin}) is −45.5 mV.[7,42] The surface potentials of APTES–PAA films ($\Psi_{APTES-PAA}$) are calculated from the zeta potential values in Fig. 5 using the Debye–Hückel equation.[42] The van der Waals interaction term is determined from the Hamaker constant between actin and

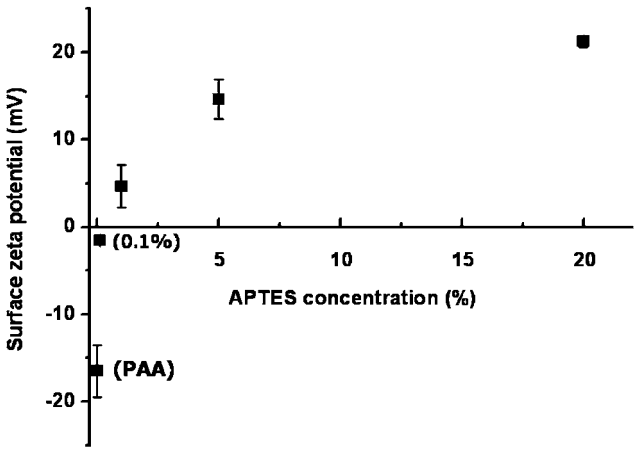

Fig. 5 Surface zeta potential of PAA and (0.1, 1, 5, and 20%) APTES–PAA films. The zeta potential increases from −16 mV to +21 mV as APTES concentration increases. This behavior demonstrates that the hydrogel surface charge converts from negative to positive upon incorporation of APTES.

APTES–PAA, A_{132}, which is taken as $\sim kT$[42] in the buffer solution.

Using the above parameters and the radius of F-actin, r_{actin} = 4 nm,[37] the total interaction energy per unit length, U_{tot}, is determined by adding the electrostatic energy per unit length, $V(H) = 2(2\pi)^{1/2}\varepsilon_{water}\varepsilon_0(\kappa r_{actin})^{1/2}[\Psi_{APTES-PAA}\Psi_{actin}\exp(-\kappa H) + 0.35\Psi^2_{APTES-PAA}(1 - 2\varepsilon_{actin}/\varepsilon_{water}(\pi\kappa r_{actin})^{-1/2})\exp(-2\kappa H) + 0.35\Psi^2_{actin}(r_{actin}/(r_{actin} + H))^{1/2}(1 - 2\varepsilon_{APTES-PAA}/\varepsilon_{water}(\pi\kappa(r_{actin} + H))^{-1/2})\exp(-2\kappa H)]$, and van der Waals energy per unit length, $W(H) = -A_{132}(2r_{actin})^{1/2}/24H^{3/2}$,[41,42]

$$U_{tot} = V(H) + W(H) \quad (1)$$

Fig. 6 plots the total interaction energy (kT per nm) as a function of distance, H (nm). For PAA and 0.1% APTES–PAA

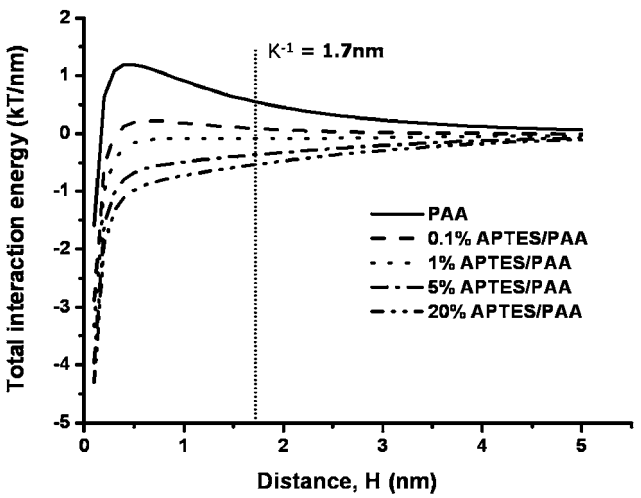

Fig. 6 Theoretical calculation of the interaction energy between F-actin and APTES–PAA films. The model is based on the electrostatic and van der Waals interactions between cylindrical actin and the planar hydrogel substrate. The total interaction energy per unit length of actin (kT per nm) is plotted as a function of the distance, H, between the substrate and the bottom of the cylinder for APTES concentrations up to 20%. The Debye screening length is 1.7 nm.

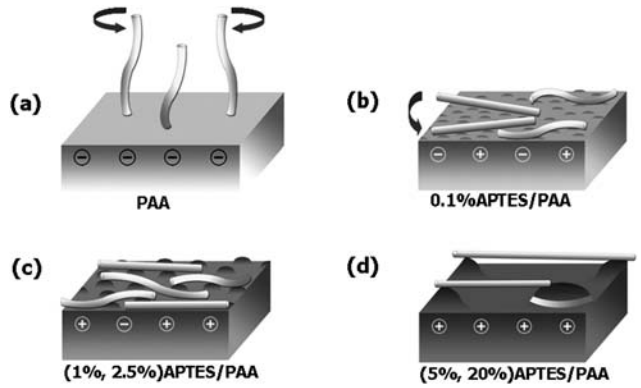

Fig. 7 Upon varying the surface charge (−, +) and topography of APTES–PAA films, the orientation, coverage, and curvature of F-actin are controlled. In (a), F-actin is tethered at one end and otherwise repelled so as to orient and wobble perpendicular to the surface, whereas in (b) as the surface charge becomes more positive, F-actin aligns parallel to the surface and fluctuates near the surface. As surface charge continues to increase, (c) F-actin coverage increases and the filaments become immobilized on the substrate. Finally, when micron-sized, positive islands form, (d) F-actin coverage decreases because they mainly attach by stretching between islands or, less frequently, forming rings that wrap around the islands.

substrates, the total interaction energy has a maximum positive value at ~0.5 nm. This barrier reflects the electrostatic repulsion at long-range. At short-range, the total energy is dominated by the attractive van der Waals interaction. For 1% APTES, 5% APTES, and 20% APTES, the total interactions are attractive at all separations. In the future, a detailed model is needed that captures the contributions of substrate topography, charge heterogeneity, and F-actin charge distribution. Nevertheless, this simple theoretical calculation qualitatively agrees with the experimental observation made in the TIRFM studies.

Based on our experiments and theoretical calculations, we propose a model describing how self-assembled charged hydrogels control the alignment of filamentous actin. On negatively charged PAA, F-actin orients perpendicular to the surface and wobbles above it because the electrostatic repulsion from the surface (*i.e.*, COO^- groups) is nearly balanced by the van der Waals attraction as represented by Fig. 7(a). Repulsion is reduced by the perpendicular orientation but the van der Waals attraction at short-range is sufficient to tether the F-actin by its end. The perpendicular orientation of the filaments at low APTES incorporation is explained by the charge repulsion but cannot be directly compared with our model which assumes a parallel orientation. With increasing surface charge, F-actin is more strongly attracted to the surface and orients parallel to the surface; however, because the strength of the attraction is weak the filament is able to fluctuate along the surface (Fig. 7(b)). At high surface charge, F-actin becomes immobilized (Fig. 7(c) and (d)) due to the strong electrostatic attraction. At 5% and 20% APTES, this increase in surface charge is confounded by the formation of micron-sized APTES-rich islands that reduce the surface coverage of F-actin relative to the smooth surfaces. Moreover, filaments are sometimes found to wrap around these islands to form rings or, more often, to stretch across two or more islands to form highly elongated molecules.

Conclusions

In conclusion, we have created self-assembled hydrogel films that control the orientation, interaction strength, surface coverage, and curvature of F-actin. This control has been achieved by tuning the surface charge and topography of APTES–PAA films. The surface coverage of F-actin reaches a maximum value at 2.5% APTES. This behavior is explained by the simultaneous increase in surface charge and formation of a microscale pattern of APTES-rich aggregates. This study provides guidelines for constructing molecular shuttle devices. For example, by controlling surface charge and topography, the perpendicular and parallel orientations of F-actin allow for motion of myosin both along the surface as well as in a third dimension (out of the surface plane). Moreover, actin filaments that are parallel and only weakly bound (*e.g.* 0.1% APTES case) are able to fluctuate, possibly facilitating track "switching" by molecular motors. These surfaces also allow one to create straight or circular tracks at the nanoscale.

Acknowledgements

This work was primarily supported by the Nano/Bio Interface Center at the University of Pennsylvania and the US National Science Foundation (NSF) under grant number DMR-0425780. Partial support was provided by NSF under grant number DMR-0549307 and DMR-0520020 and National Institute of Health under grant number GM086352. We thank Professor Daeyeon Lee (PENN) for help with the zeta potential measurements.

References

1 H. Hess, J. Clemmens, D. Qin, J. Howard and V. Vogel, *Nano Lett.*, 2001, **1**, 235–239.
2 S. Diez, C. Reuther, C. Dinu, R. Seidel, M. Mertig, W. Pompe and J. Howard, *Nano Lett.*, 2003, **3**, 1251–1254.
3 M. G. L. Van den Heuvel and C. Dekker, *Science*, 2007, **317**, 333–336.
4 D. H. Boal, *Mechanics of the Cell*, Cambridge University Press, Cambridge, 2002.
5 B. Alberts, A. Johnson, J. Lewis, M. Raff, K. Roberts and P. Walter, *Molecular Biology of the Cell*, Garland Science, New York, 4th edn, 2002.
6 A. D. Bershadsky and J. M. Vasiliev, *Cytoskeleton*, Plenum Press., New York, 1988.
7 J. X. Tang and P. A. Janmey, *J. Biol. Chem.*, 1996, **271**, 8556–8563.
8 J. X. Tang and P. A. Janmey, *Biol. Bull.*, 1998, **194**, 406–408.
9 I. Borukhov, R. F. Bruinsma, W. M. Gelbart and A. J. Liu, *Proc. Natl. Acad. Sci. U. S. A.*, 2005, **102**, 3673–3678.
10 T. E. Angelini, H. Liang, W. Wriggers and G. C. L. Wong, *Proc. Natl. Acad. Sci. U. S. A.*, 2003, **100**, 8634–8637.
11 G. C. L. Wong, A. Lin, J. X. Tang, Y. Li, P. A. Janmey and C. R. Safinya, *Phys. Rev. Lett.*, 2003, **91**, 018103-1–018103-4.
12 I. Rasnik, S. A. Mckinney and T. Ha, *Acc. Chem. Res.*, 2005, **38**, 542–548.
13 J. N. Forkey, M. E. Quinlan, M. Alexander Shaw, J. E. T. Corrie and Y. E. Goldman, *Nature*, 2003, **422**, 399–404.
14 A. Yildiz, J. N. Forkey, S. A. Mckinney, T. Ha, Y. E. Goldman and P. R. Selvin, *Science*, 2003, **300**, 2061–2065.
15 K. A. Interliggi, W. L. Zeile, S. A. Ciftan-Hens, G. E. McGuire, D. L. Purich and R. B. Dickinson, *Langmuir*, 2007, **23**, 11911–11916.
16 J. Park, Y. Sun, Y. E. Goldman and R. J. Composto, *Macromolecules*, 2009, **42**, 1017–1023.

17 M. G. L. Van den Heuvel, M. P. de Graaff and C. Dekker, *Science*, 2006, **312**, 910–914.
18 I. Y. Wong, M. J. Footer and N. A. Melosh, *Soft Matter*, 2007, **3**, 267–274.
19 L. Huang, P. Manandhar, K. Byun, P. B. Chase and S. Hong, *Langmuir*, 2006, **22**, 8635–8638.
20 L. S. Hirst, E. R. Parker, Z. Abu-Samah, Y. Li, R. Pynn, N. C. MacDonald and C. R. Safinya, *Langmuir*, 2005, **21**, 3910–3914.
21 L. Vonna, L. Limozin, A. Roth and E. Sackmann, *Langmuir*, 2005, **21**, 9635–9643.
22 D. V. Nicolau, G. Solana, M. Kekic, F. Fulga, C. Mahanivong, J. Wright and C. G. dos Remedios, *Langmuir*, 2007, **23**, 10846–10854.
23 D. V. Nicolau, H. Suzuki, S. Mashiko, T. Taguchi and S. Yoshikawa, *Biophys. J.*, 1999, **77**, 1126–1134.
24 H. Hess, *Science*, 2006, **312**, 860–861.
25 S. G. Moorjani, L. Jia, T. N. Jackson and W. O. Hancock, *Nano Lett.*, 2003, **3**, 633–637.
26 H. Hess, C. M. Matzke, R. K. Doot, J. Clemmens, G. D. Bachand, B. C. Bunker and V. Vogel, *Nano Lett.*, 2003, **3**, 1651–1655.
27 J. A. Jaber, P. B. Chase and J. B. Schlenoff, *Nano Lett.*, 2003, **3**, 1505–1509.
28 R. J. Pelham and Y. Wang, *Proc. Natl. Acad. Sci. U. S. A.*, 1997, **94**, 13661–13665.
29 I. Levental, P. C. Georges and P. A. Janmey, *Soft Matter*, 2007, **3**, 299–306.
30 A. J. Engler, L. Richert, J. Y. Wong, C. Picart and D. E. Discher, *Surf. Sci.*, 2004, **570**, 142–154.
31 A. Engle, L. Bacakova, C. Newman, A. Hategan, M. Griffin and D. Discher, *Biophys. J.*, 2004, **86**, 617–628.
32 J. Solon, I. Levental, K. Sengupta, P. C. Georges and P. A. Janmey, *Biophys. J.*, 2007, **93**, 4453–4461.
33 P. Uttayarat, G. K. Toworfe, F. Dietrich, P. I. Lelkes and R. J. Composto, *J. Biomed. Mater. Res., Part A*, 2005, **75**, 668–680.
34 H. M. Powell, D. A. Kniss and J. J. Lannutti, *Langmuir*, 2006, **22**, 5087–5094.
35 J. D. Pardee and J. A. Spudich, *Methods Cell. Biol.*, 1982, **24**, 271–289.
36 J. F. Beausang, Y. Sun, M. E. Quinlan, J. N. Forkey and Y. E. Goldman, in *Single Molecule Fluorescence Polarization* via *Polarized Total Internal Reflection Fluorescent Microscopy. In Laboratory Manual for Single Molecule Studies*, ed. I. Sialiano, Cold Spring Harbor Laboratory, Cold Spring Harbor, NY, 2007.
37 J. Howard, *Mechanics of Motor Proteins and the Cytoskeleton*, Sinauer Associates, Inc., Sunderland, MA, 2001.
38 J. X. Tang, J. A. Käs, J. V. Shah and P. A. Janmey, *Eur. Biophys. J.*, 2001, **30**, 477–484.
39 A. Cēbers, Z. Dogic and P. A. Janmey, *Phys. Rev. Lett.*, 2006, **96**, 247801-1–247801-4.
40 S. H. Choi and B. Z. Newby, *Surf. Sci.*, 2006, **600**, 1391–1404.
41 H. Ohshima, *Colloid Polym. Sci.*, 1999, **277**, 563–569.
42 J. N. Israelachvili, *Intermolecular & Surface Forces*, Academic Press., London, 2nd edn, 1992.